Lithium-Ion Battery State of Charge and Critical Surface Charge Estimation Using an Electrochemical Model-Based Extended Kalman Filter

Domenico Di Domenico
Institut Français du Pétrole (IFP),
IFP Energies Nouvelles,
Rond-Point de l'échangeur de Solaize,
B.P. 3,
69360 Solaize, Lyon, France
e-mail: didomend@ifp.fr

Anna Stefanopoulou
Department of Mechanical Engineering,
University of Michigan,
Ann Arbor, MI 48109-2121
e-mail: annastef@umich.edu

Giovanni Fiengo
Dipartimento di Ingegneria,
Università degli Studi del Sannio,
Piazza Roma 21,
82100 Benevento, Italy
e-mail: gifiengo@unisannio.it

*This paper presents a numerical calculation of the evolution of the spatially resolved solid concentration in the two electrodes of a lithium-ion cell. The microscopic solid concentration is driven by the macroscopic Butler–Volmer current density distribution, which is consequently driven by the applied current through the boundary conditions. The resulting, mostly causal, implementation of the algebraic differential equations that describe the battery electrochemical principles, even after assuming fixed electrolyte concentration, is of high order and complexity and is denoted as the full order model. The full order model is compared with the results in the works of Smith and Wang (2006, "Solid-State Diffusion Limitations on Pulse Operation of a Lithium-Ion Cell for Hybrid Electric Vehicles," J. Power Sources, **161**, pp. 628–639) and Wang et al. (2007 "Control oriented 1D Electrochemical Model of Lithium Ion Battery," Energy Convers. Manage., **48**, pp. 2565–2578) and creates our baseline model, which will be further simplified for charge estimation. We then propose a low order extended Kalman filter for the estimation of the average-electrode charge similarly to the single-particle charge estimation in the work of White and Santhanagopalan (2006, "Online Estimation of the State of Charge of a Lithium Ion Cell," J. Power Sources, **161**, pp. 1346–1355) with the following two substantial enhancements. First, we estimate the average-electrode, or single-particle, solid-electrolyte surface concentration, called critical surface charge in addition to the more traditional bulk concentration called state of charge. Moreover, we avoid the weakly observable conditions associated with estimating both electrode concentrations by recognizing that the measured cell voltage depends on the difference, and not the absolute value, of the two electrode open circuit voltages. The estimation results of the reduced, single, averaged electrode model are compared with the full order model simulation.* [DOI: 10.1115/1.4002475]

1 Introduction

Lithium-ion battery is the core of new plug-in hybrid electrical vehicles (PHEV) as well as considered in many second generation hybrid electric vehicles (HEV). Micro-macroscopic battery electrochemical modeling is connected with the hybrid vehicle design, scale-up, optimization, and control issues of HEV where the battery plays an important role in this area as high-rate transient power source. The battery models based on electrochemistry laws [1,2] are generally preferred to the equivalent circuit or to other kinds of simplified models because they also predict the physical cells limitations, which have a relevant effect in the automotive application where the battery suffers very often the stress of very high transient loads [3].

The importance of lithium-ion battery has grown in the past years. Based on the the third lightest element, this kind of battery has the right characteristics to be widely used in the hybrid vehicles, thanks to its high energy density, no memory effect, and a slow loss of charge when not in use. As the majority of advanced battery systems, lithium-ion batteries employ porous electrodes in order to increase the active area between electrolyte and solid active material, facilitating the electrochemical reactions [3–6].

Literature on electrochemical modeling of batteries is quite extensive, including both full order and simplified models. A first electrochemical approach to porous electrodes modeling for battery applications was presented by Newman and Tiedemann in Ref. [7]. In the porous electrode theory [7], the electrode is treated as a superposition of two continua, namely, the electrolytic solution and the solid matrix. The solid matrix is modeled as microscopic spherical particles where the lithium ions diffuse and react on the spheres surface. This approach was later expanded to two composite electrodes and a separator by Fuller et al. in [8]. Based on this model, Ramadass et al. in [9] accounted for the decay in capacity of the cell while Sikha et al. in [10] included the change in the porosity of the electrode material as a function of time using a pseudo-two-dimensional approach. Unfortunately, due to the irregular morphology, the electrode porosity increases the model complexity. Thus, a macroscopic description of the cell is needed. A micro-macroscopic coupled model meeting this requirement with microscopic and interfacial phenomena, as described in the porous electrode theory, rigorously and systematically integrated into a macroscopic battery model was introduced by Wang et al. in [11]. It incorporates solid-state physics and interface chemistry and can be adapted to a wide range of active materials and electrolyte solutions. Presented at the beginning for Ni-MH batteries [12], it was quickly expanded to lithium-ion batteries in [3,13] where the thermal behavior was also described. The full order electrochemical models predict the profile of solid concentration, i.e., lithium concentration in the solid phase across the electrode,

Contributed by the Dynamic Systems Division of ASME for publication in the Journal of Dynamic Systems, Measurement, and Control. Manuscript received September 29, 2008; final manuscript received March 22, 2010; published online October 29, 2010. Assoc. Editor: Loucas Louca.

during charge and discharge, but it is difficult to apply to a real-time on-board vehicle estimator due to the complexity of the model. As a consequence several approximations between the input and output of the dynamical system and the battery input and output are introduced to reduce the system order and complexity [4,14] and to allow the estimation of the battery state of charge (SOC).

The SOC estimation and regulation is one of the most important and challenging tasks for hybrid and electrical vehicle control. In fact, when the batteries operate in a relative limited range of state of charge, high efficiency, slow aging, and no damaging are expected. Several techniques have been proposed for the SOC estimation, such as equivalent circuit model-based algorithms [15,16] or black-box methods (as an example using fuzzy-logic [17]). The accuracy reached by these SOC estimations is approximately 2% [18].

Recently, the effort to use electrochemical models in order to estimate the internal state of the battery has been intensified. Starting from the model introduced by Wang in [19] a low order state variable model practical for real-time estimation and control has been obtained. In [20], based on a simplified representation of the electrode introduced by Haran et al. in [21], a Kalman filter was designed in order to estimate an average value of the bulk solid concentration.

In this paper, we employ an electrode-average concentration approximation, similar but higher order than the single-particle electrode estimation of [20]. We then present an extended Kalman filter for SOC, which typically relates to the bulk battery capacity through integration of the current drawn, although in our work it represents the average particle concentration of the average-electrode. We also estimate the critical surface charge (CSC) estimation, which is the electrode-average solid concentration at the electrolyte interface. In the following, a general micro-macroscopic lithium-ion battery model, as it is presented in [3], is summarized and a numerical solution is shown. Then, the model is simplified in order to make it compatible with a feasible solid concentration estimation. Finally, an extended Kalman filter (EKF) is designed based on the averaged model. The estimation results are compared with the high order numerical approximation of the micro-macroscopic model prediction.

2 Battery General Feature

A battery is composed of three parts: the two electrodes and the separator. Referring to a porous battery, each electrode consists of a solid matrix inside an electrolyte solution.

In particular, for a lithium-ion battery, the anode (or referring to the battery discharge, "negative electrode") is composed of carbon and the cathode (or "positive electrode" during discharge) is a metal oxide.

In the separator, the lithium-salt electrolyte is held in an organic solvent such as $LiPF_6$, $LiBF_4$, or $LiClO_4$, or in a solid polymer composite such as polyethylene oxide or poly-acrylonitrile (lithium-ion polymer battery). Both the solvent and the polymer conduct the ion but they are electronic insulators. As shown in Fig. 1, at the negative electrode, the solid active material particles of lithium of the Li_xC_6 diffuse until the electrolyte-solid interface where the chemical reaction occurs, transferring the lithium-ion to the solution and the electrons to the collector [3]. The produced electrolyte material travels through the solution to the positive electrode where, at the interface with solid material, they react and insert into the metal oxide solid particles. The chemical reactions are as follows: negative electrode reaction

$$Li_xC_6 \leftrightarrows C_6 + x\ Li^+ + x\ e^-$$

positive electrode reaction

$$Li_{y-x}Mn_2O_4 + x\ Li^+ + x\ e^- \leftrightarrows Li_yMn_2O_4$$

net reaction

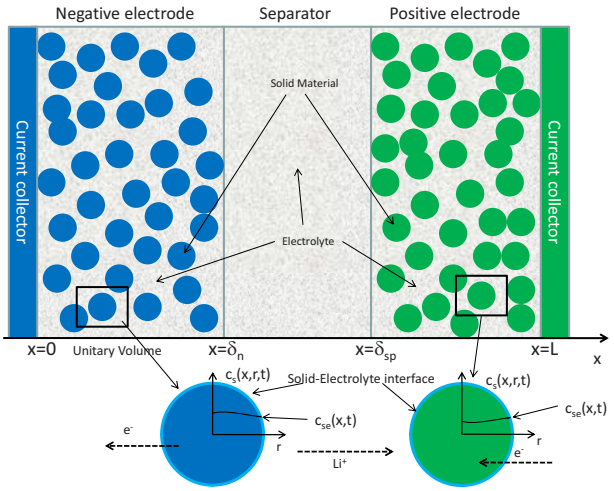

Fig. 1 Schematic macroscopic (*x*-direction) cell model with coupled microscopic (*r*-direction) solid diffusion model. The electrodes nomenclature refers to the battery discharge (reproduced from [11] and [12]).

$$Li_{y-x}Mn_2O_4 + Li_x\ C_6 \leftrightarrows Li_yMn_2O_4 + C_6$$

where the two ways of the reaction refer to the battery discharge reaction (right arrow) and to the battery charge reaction (left arrow).

The phenomena occurring at the microscale can have strong implications for the cell discharge and charge during pulse operations. However, due to the complexity of solid-electrolyte interface morphology, it is problematic to solve the equations on a microscopic scale [11]. So, in order to mathematically model the battery, both macroscopic and microscopic physics have to be considered. The equations describe the battery system with four quantities, i.e., solid and electrolyte concentrations (c_s, c_e) and solid and electrolyte potentials (ϕ_s, ϕ_e). Table 1 summarizes the nomenclature for the model development. The complete set of equation for the micro-macroscopic model is [3,13]

$$\nabla_x \kappa^{\text{eff}} \nabla_x \phi_e + \nabla_x \kappa_D^{\text{eff}} \nabla_x \ln c_e = -j^{\text{Li}} \tag{1}$$

$$\nabla_x \sigma^{\text{eff}} \nabla_x \phi_s = j^{\text{Li}} \tag{2}$$

describing the potentials distribution and

Table 1 Lithium-ion model nomenclature

Symbol	Name	Unit
i_e	Electrolyte current density	A cm^{-2}
i_s	Solid current density	A cm^{-2}
ϕ_e	Electrolyte potential	V
ϕ_s	Solid potential	V
c_e	Electrolyte concentration	mol cm^{-3}
c_s	Solid concentration	mol cm^{-3}
c_{se}	Solid concentration at electrolyte interface	mol cm^{-3}
j^{Li}	Butler–Volmer current density	A cm^{-3}
θ_n	Normalized solid concentration at anode	–
θ_p	Normalized solid concentration at cathode	–
U	Open circuit voltage	V
U_n	Anode open circuit voltage	V
U_p	Cathode open circuit voltage	V
η	Overpotential	V
F	Faraday's number	C mol^{-1}
I	Battery current	A
R	Gas constant	J K^{-1} mol^{-1}
T	Temperature	K

$$\frac{\partial \epsilon_e c_e}{\partial t} = \nabla_x (D_e^{\text{eff}} \nabla_x c_e) + \frac{1 - t^0}{F} j^{\text{Li}} \tag{3}$$

$$\frac{\partial c_s}{\partial t} = \nabla_r (D_s \nabla_r c_s) \tag{4}$$

describing the diffusion governed concentrations for the positive (p) and negative (n) electrode.

In order to simplify the model, we assume a constant electrolyte concentration c_e. This simplification can also be found in Ref. [20] and is justified due to the insignificant (<5%) variations observed in the electrolyte concentration in the detailed model [3]. Then the set of equations can be simplified by neglecting the Eq. (3) and simplifying the Eq. (1). Furthermore, introducing the solid current i_s and the electrolyte current i_e the second order partial differential equations (PDE) system for the potentials can be rewritten as

$$i_e(x) = -\kappa^{\text{eff}} \nabla_x \phi_e \tag{5}$$

$$i_s(x) = -\sigma^{\text{eff}} \nabla_x \phi_s \tag{6}$$

$$\nabla_x i_e(x) = j^{\text{Li}} \tag{7}$$

$$\nabla_x i_s(x) = -j^{\text{Li}} \tag{8}$$

with the Butler–Volmer current density

$$j^{\text{Li}}(x) = a_s j_0 \left[\exp\left(\frac{\alpha_a F}{RT} \eta \right) - \exp\left(-\frac{\alpha_c F}{RT} \eta \right) \right] \tag{9}$$

where R and F are the universal gas constant and Faraday's constant, T is the absolute temperature, and η is the overpotential, obtained as

$$\eta = \phi_s - \phi_e - U(c_{se}) \tag{10}$$

and U is the open circuit voltage, function of the solid concentration at the electrolyte interface indicated with $c_{se}(x,t) = c_s(x, R_s, t)$. The value of the concentration at the interface solid-electrolyte has a particular relevance during the cell pulse operations and it is called critical surface charge, defined as

$$\text{CSC}(t) = \frac{\theta - \theta_{0\%}}{\theta_{100\%} - \theta_{0\%}} \tag{11}$$

where $\theta = c_{se}/c_{s,\max}$ is the normalized solid-electrolyte concentration. Its reference value, $\theta_{100\%}$, can be defined for each electrode finding the concentration corresponding to a full charge battery, i.e., 100% of the state of charge. Thus, the 0% reference stoichiometry can be derived from $\theta_{100\%}$ by subtracting the battery capacity Q, with the appropriate conversion,

$$\theta_{0\%} = \theta_{100\%} - \frac{Q}{\delta} \left(\frac{1}{AF\varepsilon c_{s,\max}} \right) \tag{12}$$

where δ, ε, and $c_{s,\max}$ have appropriate values for negative and positive electrode. The open circuit voltage for the negative electrode, denoted with the subscript n, is calculated using the empirical correlation introduced in [22]

$$\begin{aligned} U_n(\theta_n) = {} & 8.0029 + 5.0647\theta_n - 12.578\theta_n^{0.5} - 8.6322 \times 10^{-4}\theta_n^{-1} \\ & + 2.1765 \times 10^{-5}\theta_n^{3/2} - 0.46016 \exp[15.0(0.06 - \theta_n)] \\ & - 0.55364 \exp[-2.4326(\theta_n - 0.92)] \end{aligned} \tag{13}$$

For the positive electrode, denoted with p, the result obtained from [3] has been adopted

$$\begin{aligned} U_p(\theta_p) = {} & 85.681\theta_p^6 - 357.70\theta_p^5 + 613.89\theta_p^4 - 555.65\theta_p^3 + 281.06\theta_p^2 \\ & - 76.648\theta_p + 13.1983 - 0.30987 \exp(5.657\theta_p^{115}) \end{aligned} \tag{14}$$

The normalized solid-electrolyte at the negative and positive electrodes are here indicated with θ_n and θ_p, respectively. The coefficient j_0 in (9) also exhibits a modest dependence on the solid and electrolyte concentrations, according to

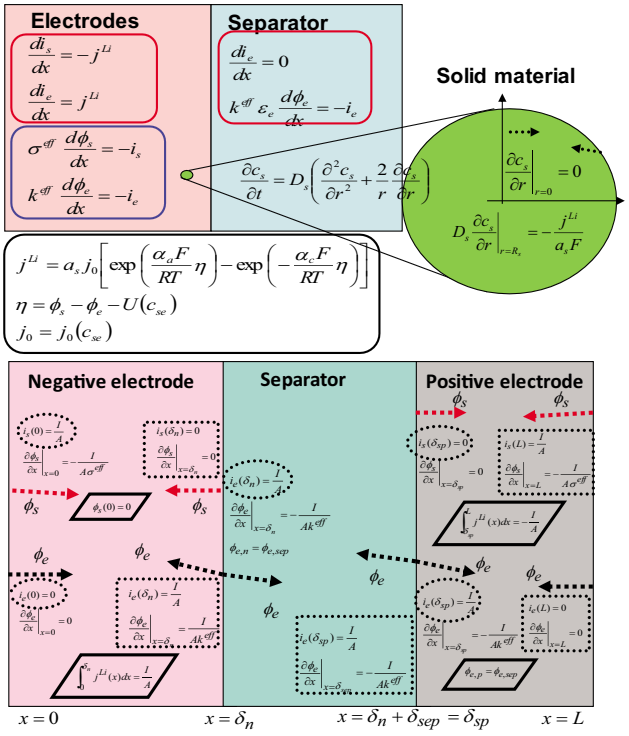

Fig. 2 Schematic representation of the set of equations and of the boundary conditions for the potentials and solid concentration. The current *I* is assumed to be positive (battery discharge) and provide boundary condition (boxes with dotted line) and the nonlocal constraints (boxes with solid line) governing the Butler–Volmer current density.

$$j_0 = (c_e)^{\alpha_a} (c_{s,\max} - c_{se})^{\alpha_a} (c_{se})^{\alpha_c} \tag{15}$$

Finally, the cell potential, which is typically measured is computed as

$$V = \phi_s(x = L) - \phi_s(x = 0) - R_f I \tag{16}$$

where R_f is the film resistance on the electrodes surface. In Fig. 2, the model equations and their boundary conditions for the x-domain and r-domain are shown. Note that the temperature spatial and temporal gradients are neglected in this work.

For completeness the battery model parameters are summarized in Table 2 and more details on the model and its parameters can be found in [3,12].

3 Numerical Solution

In order to solve the battery PDE model, the boundary conditions are necessary. At the boundary with the current collectors of the negative and positive electrode, i.e., at $x=0$ and at $x=L$ (see Fig. 1), it is

$$i_e(x = 0) = 0 \tag{17}$$

$$i_e(x = L) = 0 \tag{18}$$

$$i_s(x = 0) = \frac{I}{A} \tag{19}$$

Table 2 Battery parameters

Parameter	Negative electrode	Separator	Positive electrode
Thickness (cm)	$\delta_n = 50 \times 10^{-4}$	$\delta_{sep} = 25.4 \times 10^{-4}$	$\delta_p = 36.4 \times 10^{-4}$
Particle radius R_s (cm)	1×10^{-4}	–	1×10^{-4}
Active material volume fraction ε_s	0.580	–	0.500
Electrolyte phase volume fraction (porosity) ε_e	0.332	0.5	0.330
Conductivity of solid active material σ (Ω^{-1} cm^{-1})	1	–	0.1
Effective conductivity of solid active material	$\sigma^{eff} = \varepsilon_s \sigma$	–	$\sigma^{eff} = \varepsilon_s \sigma$
Transference number t_+^0	0.363	0.363	0.363
Electrolyte phase ionic conductivity κ (Ω^{-1} cm^{-1})	$\kappa = 0.0158 c_e \exp(0.85 c_e^{1.4})$	$\kappa = 0.0158 c_e \exp(0.85 c_e^{1.4})$	$\kappa = 0.0158 c_e \exp(0.85 c_e^{1.4})$
Effective electrolyte phase ionic conductivity	$\kappa^{eff} = (\varepsilon_e)^{1.5} \kappa$	$\kappa^{eff} = (\varepsilon_e)^{1.5} \kappa$	$\kappa^{eff} = (\varepsilon_e)^{1.5} \kappa$
Effective electrolyte phase diffusion conductivity	$\kappa_D^{eff} = \frac{2RT\kappa^{eff}}{F}(t_+^0 - 1)$	$\kappa_D^{eff} = \frac{2RT\kappa^{eff}}{F}(t_+^0 - 1)$	$\kappa_D^{eff} = \frac{2RT\kappa^{eff}}{F}(t_+^0 - 1)$
Electrolyte phase diffusion coefficient D_e (cm^2 s^{-1})	2.6×10^{-6}	2.6×10^{-6}	2.6×10^{-6}
Effective electrolyte phase diffusion coefficient	$D_e^{eff} = (\varepsilon_e)^{1.5} D_e$	$D_e^{eff} = (\varepsilon_e)^{1.5} D_e$	$D_e^{eff} = (\varepsilon_e)^{1.5} D_e$
Solid phase diffusion coefficient D_s (cm^2 s^{-1})	2.0×10^{-12}	–	3.7×10^{-12}
Maximum solid-phase concentration $c_{s,max}$ (mol cm^{-3})	16.1×10^{-3}	–	23.9×10^{-3}
Stoichiometry at 0% $\theta_{0\%}$	0.26	–	0.936
Stoichiometry at 100% $\theta_{100\%}$	0.676	–	0.442
Average electrolyte concentration $\bar{c}_e$ (mol cm^{-3})	1.2×10^{-3}	1.2×10^{-3}	1.2×10^{-3}
Change transfers coefficients α_a, α_c	0.5,0.5	–	0.5, 0.5
Active surface area per electrode unit volume a_s (cm^{-1})	$a_{s_n} = \frac{3\varepsilon_e}{R_s}$	–	$a_{s_p} = \frac{3\varepsilon_e}{R_s}$
Electrode plate area A (cm^2)	10,452	–	10,452

$$i_s(x = L) = \frac{I}{A} \tag{20}$$

because at the collector there is no electrolyte flux, and the solid current, i.e., the spatial gradient of solid potential, corresponds to the applied current density.

At $x = \delta_n$ and at $x = \delta_{sp}$, i.e., the separator-electrode interfaces, the boundary conditions are

$$i_s(x = \delta_n) = 0 \tag{21}$$

$$i_s(x = \delta_{sp}) = 0 \tag{22}$$

because no charge passes through the separator. Assuming a one-dimensional model, the sum of Eqs. (7) and (8) gives

$$\frac{d(i_s + i_e)}{dx} = 0 \tag{23}$$

which implies that the "total current" $(i_s + i_e)$ has to be constant along the cell. Furthermore, this constant value is known because the boundary conditions (17) and (19) give the constant value

$$i_s + i_e = \frac{I}{A} \tag{24}$$

which translates, considering Eqs. (21) and (22), to

$$i_e(x = \delta_n) = \frac{I}{A} \tag{25}$$

$$i_e(x = \delta_{sp}) = \frac{I}{A} \tag{26}$$

It can also be shown, integrating Eq. (7) (or, equivalently, Eq. (8)) between $x = 0$ and $x = \delta_n$, that the condition (24) is equivalent to

$$\int_0^{\delta_n} j^{Li}(x')dx' = \frac{I}{A} \tag{27}$$

as expected because the total current generated by the microscopic chemical reactions is the integral along the cell of the microscopic current density flux. The same condition can be found for the positive electrode

$$\int_{\delta_{sp}}^{L} j^{Li}(x')dx' = -\frac{I}{A} \tag{28}$$

By the way, the Eqs. (5)–(8) are two second order PDEs with two sets of boundary conditions defining the slopes at the boundary. Hence, the distribution shape of the potentials can be found but not its absolute value. To provide the complete solution for $\phi_e(0 < x < \delta_n)$ and $\phi_s(0 < x < \delta_n)$, we first assume $\phi_s(x = 0) = 0$ and then we find $\phi_e(x = 0)$ by using the constrain given in the (27). Similarly, to find the potentials $\phi_e(\delta_{sp} < x < L)$ and $\phi_s(\delta_{sp} < x < L)$, we apply the corresponding constrain for the positive electrode, i.e., Eq. (28).

Regarding the solid active material, the boundary conditions connect the concentration with the chemistry of the reactions through the surface microscopic current density. So the boundary condition at $r = 0$ is

$$\left.\frac{\partial c_s(x,t)}{\partial r}\right|_{r=0} = 0 \quad \forall\, x \tag{29}$$

and at $r = R_s$, the boundary conditions are

$$D_s \left.\frac{\partial c_s(x,t)}{\partial r}\right|_{r=R_s} = -\frac{j^{Li}(x,t)}{a_{s_p} F} \tag{30}$$

for positive electrode's particles

$$D_s \left.\frac{\partial c_s(x,t)}{\partial r}\right|_{r=R_s} = -\frac{j^{Li}(x,t)}{a_{s_n} F} \tag{31}$$

for negative electrode's particles.

Finally, in Fig. 2, the complete set of equations is provided and a graphical representation of the boundary conditions for x-domain and r-domain is shown.

The lithium-ion PDE system with its initial and boundary conditions was simulated and numerically solved in the MATLAB/SIMULINK environment by using the finite difference method. To reproduce the spatial dependence of the model variables, the currents (i_s and i_e), the potential (ϕ_s and ϕ_e) and the Butler–Volmer current j^{Li} were spatially discretized and the differential Eqs. (5)–(8), with the Eq. (9), were solved using the finite difference method. Referring to the negative electrode, let N_x the number of

discretization steps. The algebraic variables, depending on time, are $\phi_{s_l}(t)$, $\phi_{e_l}(t)$, $i_{s_l}(t)$, $i_{e_l}(t)$, and $j_l^{\mathrm{Li}}(t)$, and the algebraic system, to be solved each simulation step, is

$$i_{s_l} = i_{s_{l-1}} - j_{l-1}^{\mathrm{Li}} * \Delta_x$$

$$i_{e_l} = i_{e_{l-1}} + j_{l-1}^{\mathrm{Li}} * \Delta_x$$

$$\Phi_{s_l} = \Phi_{s_{l-1}} - \frac{1}{\sigma^{\mathrm{eff}}} i_{s_{l-1}} \Delta_x$$

$$\Phi_{e_l} = \Phi_{e_{l-1}} - \frac{1}{k^{\mathrm{eff}}} i_{e_{l-1}} \Delta_x$$

$$\eta_l = \Phi_{s_l} - \Phi_{e_l} - U(c_{se})$$

$$j_l^{\mathrm{Li}} = a_s j_0(c_{se}) \left[\exp\left(\frac{\alpha_a F}{RT} \eta_l \right) - \exp\left(-\frac{\alpha_c F}{RT} \eta_l \right) \right] \tag{32}$$

with $l=1,\ldots,N_x$ and $\Delta_x=\delta_n/(N_x-1)$.

Critical are the boundary condition at $l=1$. Equations (17) and (19) give an initial input to recursively solve Eq. (32) with respect to currents i_s and i_e, but to solve the whole system the values of the potentials at $x=0$ are needed. As discussed above, we fix $\phi_s(x=0)=0$.

With this assumption, the problem is how to find the correct electrolyte potential value at the collector, i.e., $\phi_e(x=0)$, satisfying one of the equivalent conditions (21) and (25) or (27). The solution has been obtained by numerically minimizing $|i_S(\delta_n)|$ via a MATLAB/SIMULINK optimization tool. Note that if the dependence of the Butler–Volmer current on the solid concentration is not neglected, the model needs the optimization of the parameter $\phi_e(x=0)$ at each simulation step.

The input of the algebraic recursive system (32) is the battery current I while the solid concentration can be considered as a set of parameters that, as we are going to show, can be derived starting from the Butler–Volmer current.

The dependence of the solid concentration $c_s(r,x,t)$ on x can be described by applying the same discretization procedure that turns into $c_{s_l}(r,t)$, with $l=1,\ldots,N_x$. For each l, the partial differential (4) governs the r-dependent c_{s_l} behavior. For a state-space formulation of the solid concentration diffusion equations, let the battery current I be the model input, which governs the boundary conditions of (5)–(8) as shown in Fig. 2. For each x-dimension discretization step, an ordinary differential equation (ODE) is obtained by using the finite difference method for the r variable [23]. This results in $2N_x$ different systems (N_x for the negative and N_x for the positive electrode), each of (M_r-1)-order, driven by a time-dependent nonlinear function of the battery input I through the Butler–Volmer current. Making explicit the r-derivative in (4), it is

$$\frac{\partial c_s}{\partial t} = D_s \left(\frac{\partial^2 c_s}{\partial r^2} + \frac{2}{r} \frac{\partial c_s}{\partial r} \right) \tag{33}$$

By dividing the solid material sphere radius in M_r-1 intervals, with M_r large enough, of size $\Delta_r=R_s/(M_r-1)$, the first and the second derivative can be approximated with the finite difference. So the partial differential equation becomes

$$\frac{dc_{s_q}}{dt} = D_s \left[\frac{1}{\Delta_r^2} (c_{s_{(q+1)}} + c_{s_{(q-1)}}) - \frac{2}{\Delta_r^2} c_{s_q} + \frac{1}{\Delta_r} \frac{1}{r_q} (c_{s_{(q+1)}} - c_{s_{(q-1)}}) \right] \tag{34}$$

with $q=1,\ldots,M_r-1$ and $r_q=q\Delta_r$. The boundary conditions can be rewritten linearly, approximating the dependence of c_s on r at center,

$$c_{s_0} = c_{s_1}$$

$$c_{s_{M_r}} = c_{s_{(M_r-1)}} - \Delta_r \frac{j_l^{\mathrm{Li}}}{F a_s D_s} \tag{35}$$

The discretized PDE system at the l location along the x-dimension forms the l-state $\mathbf{c_s}=(c_{s_1}, c_{s_2}, \ldots, c_{s_{M_r-1}})^T$ showing explicitly the dependency on the Butler–Volmer current j_l^{Li},

$$\dot{c}_{s_q} = \left(\frac{q+1}{q} \right) \alpha_1 c_{s_{q+1}} - 2\alpha_1 c_{s_q} + \left(\frac{q-1}{q} \right) \alpha_1 c_{s_{q-1}}$$

$$\dot{c}_{s_{M_r-1}} = \left(\frac{M_r-2}{M_r-1} \right) \alpha_1 c_{s_{M_r-2}} - \left(\frac{M_r-2}{M_r-1} \right) \alpha_1 c_{s_{M_r-1}} - \left(\frac{M_r}{M_r-1} \right) \alpha_2 j_l^{\mathrm{Li}} \tag{36}$$

with $q=1,\ldots,M_r-2$, $l=1,\ldots,N_x$, $\alpha_1=D_s/\Delta_r^2$, $\alpha_2=1/Fa_s\Delta_r$, and $j_l^{\mathrm{Li}}(c_{se},I)=\mathcal{U}_l(c_{se},I)$, where the dependence on the input I of the Butler–Volmer current, through the (32), is explicitly highlighted. It follows

$$\dot{\mathbf{c}}_\mathbf{s} = \mathbf{A}\mathbf{c_s} + b\mathcal{U}_l \tag{37}$$

where $\mathbf{A}$ and b can be determined from (36) and the $\mathcal{U}_l$ can be considered as a set of N_x parameters, each of them appearing in one of the respective N_x state-space systems and has to be derived from (5)–(8). The output of the system is the value of the solid concentration on the sphere radius that can be rewritten as

$$c_{se} = c_{s_{M_r-1}} - \frac{\alpha_2}{\alpha_1} \mathcal{U}_l(\mathbf{c_s}, I) \tag{38}$$

These equations show that solid concentrations and potentials are related through the Butler–Volmer equation through the boundary condition. Furthermore, along each electrode, as the boundary condition, i.e., the input $\mathcal{U}_l$, depends on x the system output c_{se} is also function of x.

For the positive electrode the same procedure was applied. Also in that case, one needs to fix the boundary conditions at the collector, so the optimization tool was used to find the value of $\phi_s(L)$ that satisfies the condition on the solid current at $x=L$. On the contrary, at the separator, the discretization can be avoided and the analytical solutions can be obtained. For $\delta_n<x<\delta_{sp}$, the current of the solid material is zero; hence, the electrolyte current has to be

$$i_e = \frac{I}{A} \tag{39}$$

to satisfy the Eq. (24). Thus, using Eqs. (25) and (26), it is

$$\phi_e(x) = \phi_e(\delta_n) - \frac{I}{Ak^{\mathrm{eff}}} x \tag{40}$$

Equations (39) and (40) were used in the simulation.

4 Simulation of Full Order Model

It is difficult to validate the micro-macroscopic battery model; hence, we repeat the test presented in [3] where the model was validated with a current profile according to FreedomCAR test procedure, an U.S. Department of Energy program for the zero-emission vehicle and technology research, as reported in [24]. The test procedures, shown in the top plot of Fig. 3, consist of a 30 A battery discharge for 18 s, an open circuit relaxation for 32 s, and a 22.5 A charge for 10 s followed by open circuit relaxation. Figure 3 is inspired by [3] and tried to reproduce the numerical solution used to validate the model. In [3], the battery voltage prediction for several battery SOC initial conditions is shown. The initial SOC can be related with the initial conditions on the solid

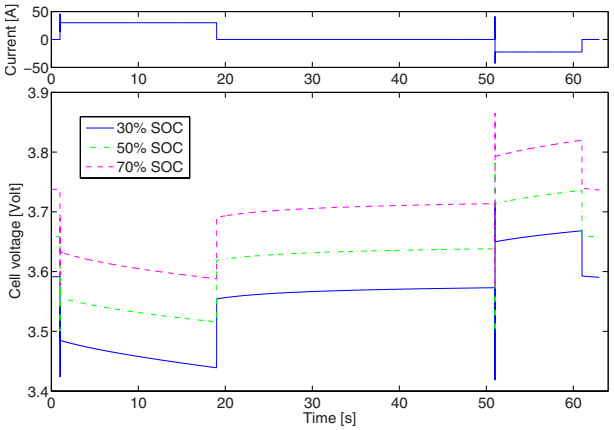

Fig. 3 Battery voltage prediction. SOC initial conditions used in the model vary from 30% to 70% of the total charge.

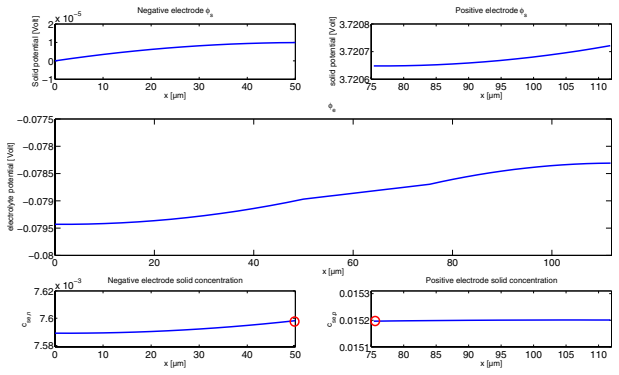

Fig. 5 Numerical solution during charge referring to a current $I=-25$ A after 3 s (i.e., after 55 s of the FreedomCAR test). The solid concentration critical point for electrodes depletion/saturation is highlighted with a circle.

concentration by introducing the stoichiometry ratio $\theta_b = \bar{c}_{sb}/c_{s,\max}$, where $\bar{c}_{sb}$ is the average bulk concentration that can be obtained as

$$\bar{c}_{sb} = \frac{3}{R^3}\int_0^{R_s} r^2 c_s(r,t)\,dr \tag{41}$$

Then, the state of charge of the battery is, with a good approximation, linearly varying with θ_b between the two stoichiometry values $\theta_{0\%}$ and $\theta_{100\%}$

$$\mathrm{SOC}(t) = \frac{\theta_b - \theta_{0\%}}{\theta_{100\%} - \theta_{0\%}} \tag{42}$$

We here assume, according to [3], a single cell with a nominal capacity $Q=6$ A h, and, for simplicity, we set uniform initial conditions on the solid concentration.

Figures 4 and 5 show the solid and electrolyte potential and the solid material concentration during the battery discharge and charge. The figures refer to the 50% SOC line in Fig. 3. In detail, the discharge refers to a battery current $I=30$ A after 2 s (i.e., after 4 s of whole test) and the charge refers to a current $I=-25$ A after 3 s (i.e., after 55 s of the whole test). Note that the potential profiles during the discharge agree with the slope imposed by the boundary conditions.

Figures 4 and 5 point out that the solid concentration is a function of the position along the electrodes. The critical values for electrodes depletion and saturation effects are the lowest one for the ion-production electrode and the highest one for the ion-insertion electrode. Because of the solid concentration profile during charge and discharge, as shown in Figs. 4 and 5, the critical points are $x=\delta_n$ and $x=\delta_{sp}$ both during discharge and during the charge.

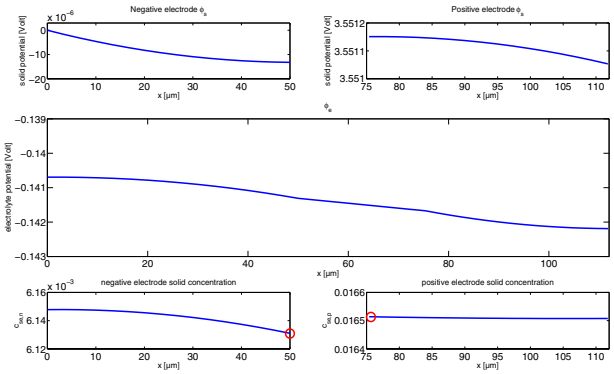

Fig. 4 Numerical solution during discharge referring to a battery current $I=30$ A after 2 s (i.e., after 4 s of the FreedomCAR test). The solid concentration critical point for electrodes depletion/saturation is highlighted with a circle.

5 Average Model

A model simplification can be provided neglecting the solid concentration distribution along the electrode and considering the material diffusion inside a representative solid material particle for each electrode. This approximation leads to an average value of the solid concentration that can be related with the definition of battery state of charge and of critical surface concentration. Although this simplified model results in a heavy loss of information, it can be useful in control and estimation applications and still maintains a small connection with the physical phenomena and dimensions [25].

In accordance with the average solid concentration, the spatial dependence of the Butler–Volmer current is ignored and a constant value $\bar{j}^{\mathrm{Li}}$ is considered, which satisfies the spatial integral (27), giving for the negative electrode (and can be reproduced accordingly in the positive electrode, considering Eq. (28))

$$\int_0^{\delta_n} j^{\mathrm{Li}}(x')\,dx' = \frac{I}{A} = \bar{j}_n^{\mathrm{Li}}\delta_n \tag{43}$$

where δ_n is the negative electrode thickness, as shown in Fig. 1.

The battery voltage (16), using Eq. (10), can be rewritten as

$$V(t) = \eta(L,t) - \eta(0,t) + (\phi_e(L,t) - \phi_e(0,t)) + (U_p(c_{se}(L,t)) - U_n(c_{se}(0,t))) - R_f I \tag{44}$$

and using the average values at the negative and the positive electrode instead of the boundary values, the following relation is obtained:

$$V(t) = \bar{\eta}_p - \bar{\eta}_n + (\bar{\phi}_{e,p} - \bar{\phi}_{e,n}) + (U_p(\bar{c}_{se,p}) - U_n(\bar{c}_{se,n})) - R_f I \tag{45}$$

Using the microscopic current average values and imposing the boundary conditions and the continuity at the interfaces, the solutions of Eqs. (5)–(8) are, for the negative electrode

$$\phi_e(x) = \phi_e(0) - \frac{I}{2Ak^{\mathrm{eff}}\delta_n}x^2 \tag{46}$$

$$\phi_s(x) = -\frac{I}{A\sigma^{\mathrm{eff}}}\left(x - \frac{x^2}{2\delta_n}\right) \tag{47}$$

for the separator

$$\phi_e(x) = \phi_e(0) - \frac{I}{2Ak^{\text{eff}}}\delta_n - \frac{I}{Ak^{\text{eff}}}(x - \delta_n) \tag{48}$$

which correspond with Eq. (40) with value of $\phi_e(\delta_n)$ computed by Eq. (46) and for the positive electrode,

$$\phi_e(x) = \phi_e(0) - \frac{I}{2Ak^{\text{eff}}}\delta_n - \frac{I}{Ak^{\text{eff}}}\delta_{\text{sep}} + \frac{I}{2Ak^{\text{eff}}\delta_p}(x - \delta_{sp})^2 - \frac{I}{Ak^{\text{eff}}}(x - \delta_{sp}) \tag{49}$$

$$\phi_s(x) = \phi_s(L) + \frac{I\delta_p}{2\sigma^{\text{eff}}A} - \frac{I(x - \delta_{sp})^2}{2\sigma^{\text{eff}}A\,\delta_p} \tag{50}$$

where $\delta_{\text{sep}} = \delta_{sp} - \delta_n$ is the separator thickness. The approximate solutions (46) and (49) lead to

$$\bar{\phi}_{e,p} - \bar{\phi}_{e,n} = \phi_e(L) - \phi_e(0) = -\frac{I}{2A}\left(\frac{\delta_n}{k^{\text{eff}}} + 2\frac{\delta_{\text{sep}}}{k^{\text{eff}}} + \frac{\delta_p}{k^{\text{eff}}}\right) \tag{51}$$

Furthermore, considering

$$\bar{j}_n^{\text{Li}} = \frac{I}{A\,\delta_n} = a_s j_0\left[\exp\left(\frac{\alpha_a F}{RT}\,\bar{\eta}_n\right) - \exp\left(-\frac{\alpha_c F}{RT}\,\bar{\eta}_n\right)\right] \tag{52}$$

$$\bar{j}_p^{\text{Li}} = -\frac{I}{A\,\delta_p} = a_s j_0\left[\exp\left(\frac{\alpha_a F}{RT}\,\bar{\eta}_p\right) - \exp\left(-\frac{\alpha_c F}{RT}\,\bar{\eta}_p\right)\right] \tag{53}$$

where $\bar{\eta}_n$ and $\bar{\eta}_p$ can be estimated as

$$\bar{\eta}_n = \frac{RT}{\alpha_a F}\ln\left(\xi_n + \sqrt{\xi_n^2 + 1}\right) \tag{54}$$

$$\bar{\eta}_p = \frac{RT}{\alpha_a F}\ln\left(\xi_p + \sqrt{\xi_p^2 + 1}\right) \tag{55}$$

where

$$\xi_n = \frac{\bar{j}_n^{\text{Li}}}{2a_s j_0} \quad \text{and} \quad \xi_p = \frac{\bar{j}_p^{\text{Li}}}{2a_s j_0} \tag{56}$$

Finally, the battery voltage (45) can be written as a function of battery current and of the average solid concentration,

$$V(t) = \frac{RT}{\alpha_a F}\ln\frac{\xi_n + \sqrt{\xi_n^2 + 1}}{\xi_p + \sqrt{\xi_p^2 + 1}} + \bar{\phi}_{e,p} - \bar{\phi}_{e,n} + (U_p(\bar{c}_{se,p}) - U_n(\bar{c}_{se,n})) - R_f I \tag{57}$$

Thus, the averaging Butler–Volmer current leads to consider a representative solid material particle somewhere along the negative and positive electrode. This simplified model has similarities with the "single-particle" model introduced in Ref. [8]. In Ref. [8], the diffusion dynamics are approximated with a first order ODE, whereas in the electrode-average model a $(M_r - 1)$-order ODE is used. Furthermore, in the electrode-average model, the cell voltage depends, through U_n and U_p, on the solid-electrolyte concentration instead of the average single-particle bulk concentration.

Figures 6–10 demonstrate the performance of the reduced order model driven by the $(M_r - 1)$-order ordinary differential Eq. (37), comparing the simulated signal with the full order model given by Eq. (37) resolved at N_x locations across the x-direction. In particular, Fig. 6 shows a good cell voltage prediction at different discharge rates from 10 A to 300 A. The depletion and saturation effects, respectively for negative and positive electrode, are evident for higher discharge rate where a sudden drop of initial SOC and cell voltage can be noticed. Note that the average voltage response reproduces the full order model numerical solution with comparable precision for different discharge rates and SOC levels. Figure 7 show a good battery voltage prediction during a FreedomCAR test procedure with a maximum error of 0.3 mV for

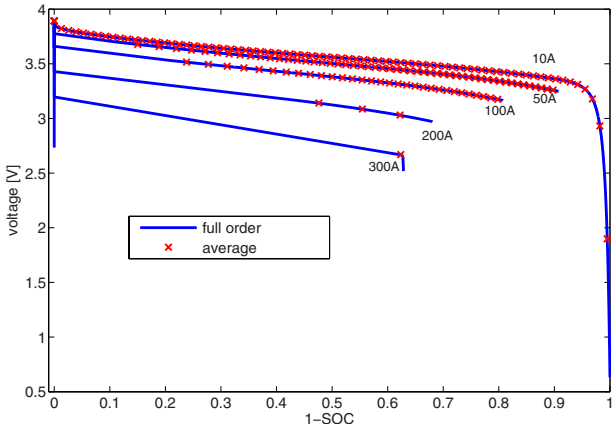

Fig. 6 Voltage response of average versus full order model for different constant current from 10 A to 300 A

the considered charge and discharge rate. Figure 8 shows the temporal distribution of solid concentration, highlighting a good agreement between the distributed value of the solid concentration and the predicted average. Figure 9 shows the error between the average solid concentration and the solid concentration at the electrodes depletion/saturation effects critical points, i.e., the electrodes-separator interfaces, as it is predicted by the full order model. Figure 10 shows the spatial distribution of electrodes solid

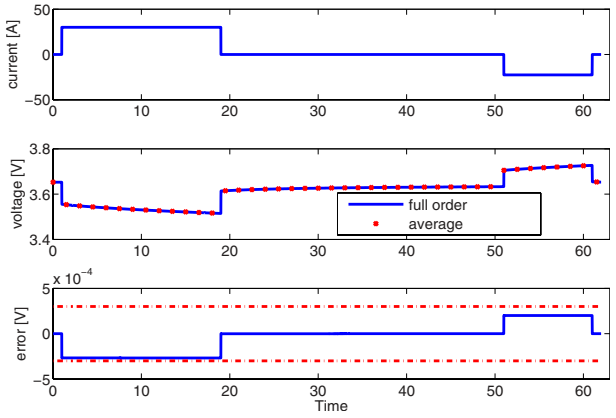

Fig. 7 Average versus full order model

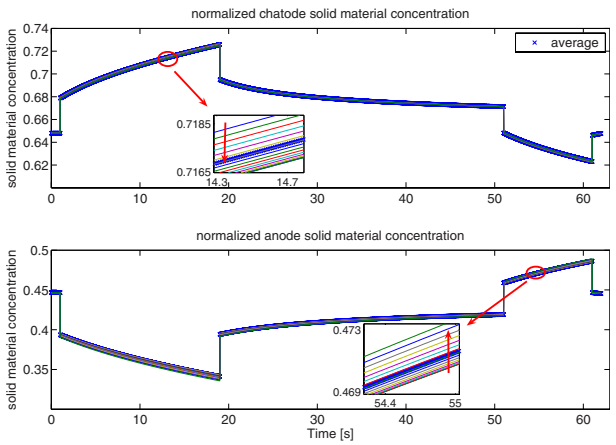

Fig. 8 Average versus full order battery model: negative and positive electrode solid material concentration. The different lines represent the concentration values along the *x*-direction.

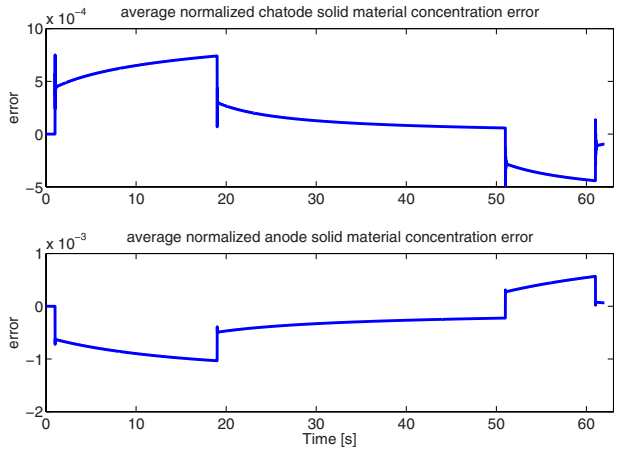

Fig. 9 Average versus full order battery model: error between the average solid concentration and the solid concentration at the electrodes-separator interface

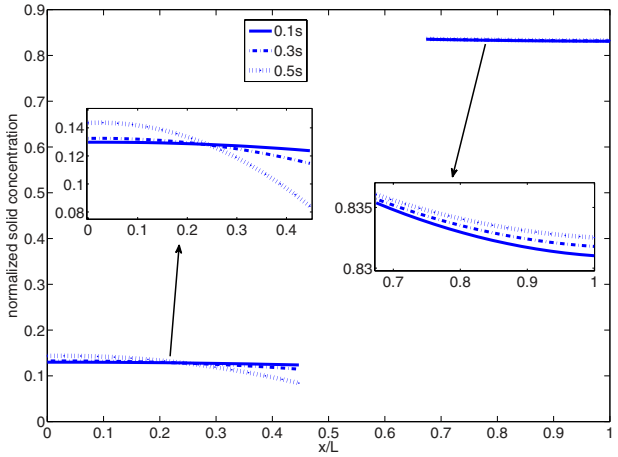

Fig. 11 Spatial distribution of electrode solid surface concentration during pulse operation at various time (0.1 s, 0.3 s, and 0.5 s) during a 180 A discharge and its error with respect to the average model prediction

surface concentration at various times during a 30 A discharge (constant for the average model) and the error introduced by averaging the spatial distribution with the average solid concentration value. Finally, Fig. 11 highlights, particularly for the negative electrode, that the solid material depletion is deeper during the pulse operations, implying an unavoidable degradation of the average model performance. The predicted gradient in solid surface concentration throughout the electrode here is smaller that the ones shown in [19] but as far as we know, nobody has really shown experimentally what the exact spatio-temporal profile of the Li-ion concentrations is.

6 Kalman Filter State of Charge Estimation

In most cases the battery voltage is measured and along the known input (current demanded), one needs to estimate the battery SOC and CSC. The physical quantity related to the battery charge is the solid concentration at the electrodes. As the solid concentration is a function of the position along the electrodes, the critical values for the state of charge estimation, able to predict correctly the electrodes depletion and saturation effects, are the lowest one for the ion-production electrode and the highest one for the ion-insertion electrode. Unfortunately, a spatially resolved concentration estimation cannot be probably realized in real-time due to the iterative process involved in the 300-state numerical solution for the full order model. A solid concentration estimation that predicts the critical concentration levels would have been more elegant. Unfortunately, the key feature of SOC estimation relies on the Butler–Volmer current values at the electrode borders. The microscopic current is not measurable, so it should be derived from the battery current by solving the PDEs (5)–(8) or the discretized equivalent (30) and (35) $2N_x$ times, which is similarly intractable. Instead, we explore the estimation using the averaged model of Sec. 5.

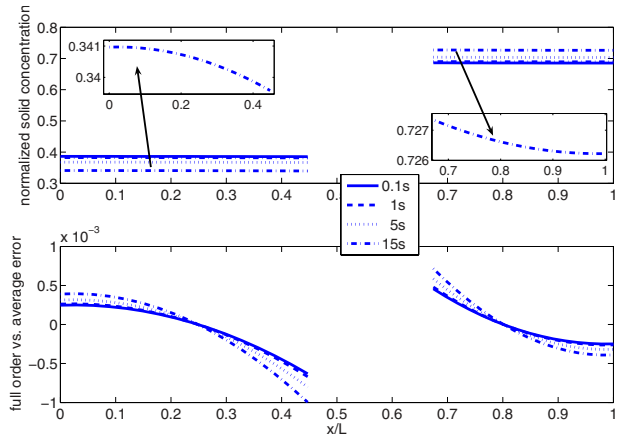

Fig. 10 Average versus full order battery model: spatial distribution of electrode solid surface concentration at various time (0.1 s, 1 s, 5 s, and 15 s) during a 30 A discharge and its error with respect to the average model prediction

Specifically, the average dynamical system describes the diffusion effects into two solid material particles, one for the positive electrode and one for the negative electrode and allows the computation of the solid concentration at the spheres radius, which represents an average value of the solid concentration along the electrodes. However the cell voltage (33) depends on $(U_p(\bar{c}_{se,p}) - U_n(\bar{c}_{se,n}))$ making the difference of the open circuit voltage observable but does not necessarily guarantee the observability of each open circuit voltage. Indeed, the system that includes both positive and negative electrode concentration states is weakly observable (in the linear sense) from the output cell voltage.

It is possible to find a relation between the positive and negative electrode-average solid concentrations, which can be used for the estimation of the negative electrode concentration based on the positive electrode. As it is shown below, the positive electrode concentration states are observable from the output cell voltage. Then, the voltage measurement is used to compute the voltage prediction error and it is then fed back to the positive (alone) electrode concentration observer. The enabling relation for realizing the negative electrode concentration as a function of the positive electrode concentration can be found in the SOC definition introduced in Eq. (42). In particular, we assume equal average solid concentration of both electrodes and allow the SOC estimation using a single averaged electrode solid concentration, even though it would have been safer to estimate SOC based on the most critical level of the solid concentration along the electrode, which can be at the electrode ends and not in the middle. By assuming that the SOC value is equal at the two electrodes, using Eq. (42), the negative electrode concentration can be computed as function of positive electrode concentration as

$$\bar{c}_{se,n} = c_{s,\max,n}\left(\theta_{n0\%} + \frac{\bar{c}_{se,p} - \theta_{p0\%}c_{s,\max,p}}{(\theta_{p100\%} - \theta_{p0\%})c_{s,\max,p}}(\theta_{n100\%} - \theta_{n0\%})\right) \tag{58}$$

where $\theta_{n0\%}$, $\theta_{n100\%}$, $\theta_{p0\%}$, and $\theta_{p100\%}$ are the reference stoichiometry points for the negative and the positive electrode.

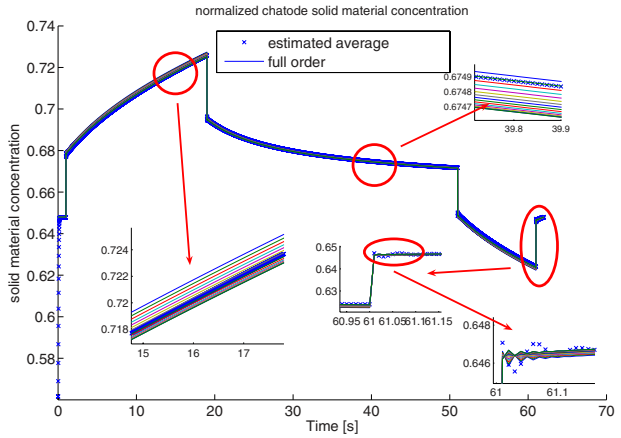

Fig. 12 Kalman filter: solid concentration estimation

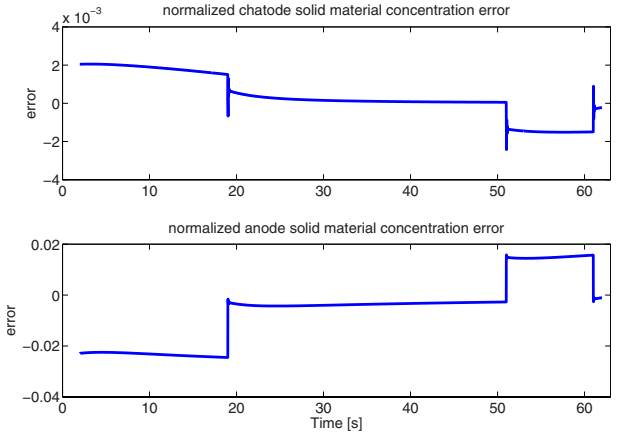

Fig. 13 Kalman filter: error between the average solid concentration estimation and full order model prediction at the electrolytes-separator interface. The transient in the EKF estimation is not shown.

Hence, introducing the state vector $x=(\bar{c}_{s,p1},\bar{c}_{s,p2},\ldots,\bar{c}_{s,p(M_r-1)})^T$, the dynamical system is

$$\dot{x}=A_p x(t)+B_p u(t) \quad \text{with } u=\bar{j}_p^{\text{Li}} \text{ and } y=V(x,u) \tag{59}$$

where the matrices A_p and B_p are obtained from Eq. (36) with reference to the positive electrode. For a linear state-space formulation, the linearized battery voltage results in an output matrix $C=\partial V/\partial x$, which is a row matrix with zeros in its first M_r-2 elements and the last nonzero term being

$$\frac{\partial V}{\partial \bar{c}_{s,p(M_r-1)}}=\frac{\partial U_p}{\partial \bar{c}_{s,p(M_r-1)}}-\frac{\partial U_n}{\partial \bar{c}_{se,n}}\frac{\partial \bar{c}_{se,n}}{\partial \bar{c}_{s,p(M_r-1)}} \tag{60}$$

due to the fact that the battery potential V is only a function of the solid concentration at interface. This output matrix C leads to a strongly observable system.

The nonlinear system observability was also studied. Equation (59) leads to a (M_r-1)-dimensional codistribution $\mathcal{H}$ of the observation space H, which imply that the system is strongly locally observable $\forall \bar{c}_{se,p}\neq 0$ [26].

Based on the average model developed in the previous section, a Kalman filter can be designed according to

$$\dot{\hat{x}}=A_p\hat{x}+Bu+K_e(y-\hat{y})$$

$$\hat{y}=V(\hat{x},u) \tag{61}$$

where $\hat{x}$ and $\hat{y}$ are the estimated state and output, respectively, V is the output nonlinear function in Eq. (57), A_p and B_p are the matrices describing the dynamical system defined in Eq. (59), C is defined in Eq. (60), and K_e is the Kalman gain, obtained as follows

$$K_e=PCR^{-1} \tag{62}$$

where P is the solution of the Riccati equation

$$\dot{P}=A_pP+PA_p^T-PCR^{-1}C^TP+Q$$

$$P(0)=P_0 \tag{63}$$

and Q and R are weight matrices appropriately tuned.

Note that one of the main advantage of the filter proposed in this paper is that the bulk and the interface solid concentration are estimated, allowing the estimation of both the CSC and the SOC.

Figures 12–17 highlight the filter performance. In particular, Figs. 16 and 17 show the simulation results for some reasonable choice of Q and R when band-limited white noise is added to the battery current and voltage in order to simulate the sensors noise. More noisy (and less expensive sensors) will require more filtering, which will slow down the estimation rate and future work on an experimental battery needs to address these issues. The fourh order Kalman filter estimation results are compared with the full 300th order model. The error in the initial condition, close to 10%, is fully and quickly recovered, showing that the filter is able to estimate the correct value of the battery state of charge even if its

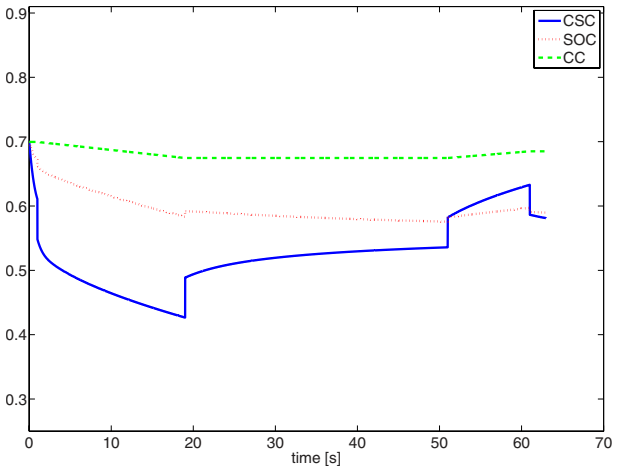

Fig. 14 Kalman filter: CSC and SOC estimations compared with the coulomb counting SOC

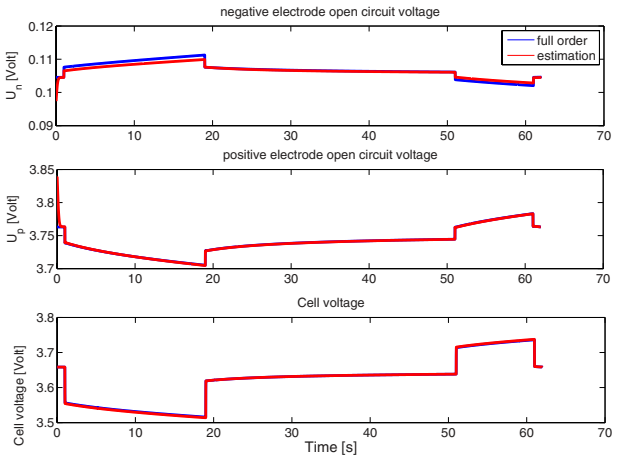

Fig. 15 Kalman filter: open circuit voltage estimation

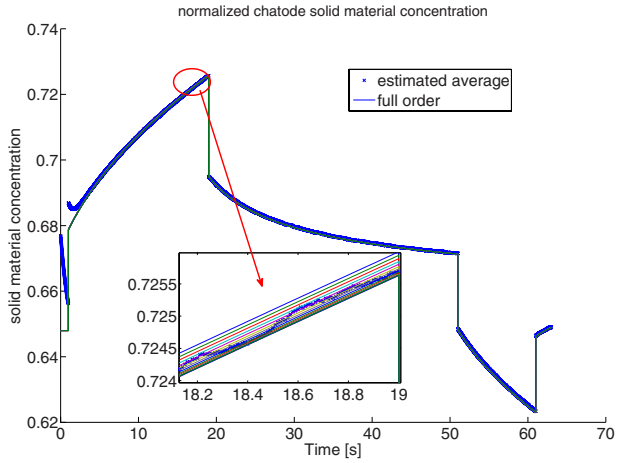

Fig. 16 Kalman filter: solid concentration estimation when noise is added to the measurements

open loop model prediction was 10% wrong. The step in current demand results in a step in solid concentration, which is again estimated by the filter, as shown in a zoom of the same figure. In particular, the Fig. 13 shows explicitly the error between the estimated solid concentration and the solid concentration depletion/saturations critical values, which are the interesting quantities to estimate for a refined estimation. It is shown that the error is less than $\pm 0.4\%$ and $\pm 3.0\%$ in the positive and negative electrodes, respectively. The negative electrode has higher prediction errors than the positive electrode due to the lack of direct observability from the voltage prediction error. In Fig. 14, the estimation of the CSC and SOC is compared with coulomb counting (CC) that evaluates the battery charge with the integral of battery current. As it is shown, the CC is unable to recover the error in the initial conditions. Figure 14 also highlights that the discontinuity in the CSC during the current steps, which is slowly recovered due to the diffusion into the particle, is only partially observable through the SOC estimation.

Furthermore, the reduced order model-based Kalman filter provides also a good estimation for the single electrode open circuit voltage even though just the open circuit voltage $U_p - U_n$ is observable. This accuracy is accomplished because the measured output V is not very sensitive to U_n, so the correct value of the battery voltage can be predicted uniquely by the positive electrode solid concentration, as confirmed by the results shown in Fig. 15.

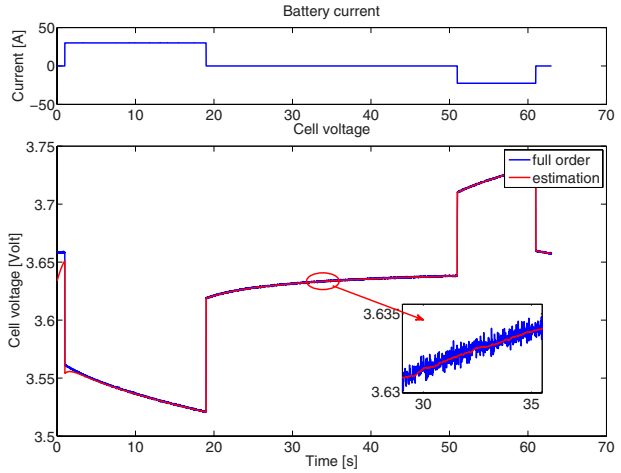

Fig. 17 Kalman filter: cell voltage estimation when noise is added to the measurements

Figures 16 and 17 show that the filter performance is barely affected by the measurement imprecision. Introducing the sensors noise into the simulation, in fact, increases the estimation convergence time and reduce the precision. However, the performance is still satisfying.

7 Conclusion

An isothermal numerical calculation of the solid concentration evolution in the two electrodes of a lithium-ion battery cell driven by a spatially distributed Butler–Volmer current was presented. The numerical solution is implemented in MATLAB/SIMULINK using the finite difference method. The isothermal electrochemical model of the lithium-ion battery cell was then used to derive an averaged model coupling, the average microscopic solid material concentration with the average values of the chemical potentials, electrolyte concentration, and current density. The full and the reduced order models were then compared and simulation results were shown and discussed. Finally, an EKF, based on the electrode-average model, was designed for the CSC and SOC estimation. Using a typical discharge followed by a charge test the estimation results show a $\pm 0.4\%$ and $\pm 3.0\%$ error in predicting the critical solid concentrations in the positive and negative electrode, respectively.

Acknowlegdment

A.S. is supported by the NSF under Grant Nos. CMS-GOALI 0625610 and CBET-GOALI 0932509.

References

[1] Doyle, M., Fuller, T. F., and Newman, J., 1993, "Modeling of Galvanostatic Charge and Discharge of the Lithium/Polymer/Insertion Cell," J. Electrochem. Soc., **140**, pp. 1526–1533.
[2] de Vidts, P., Delgado, J., and White, R. E., 1995, "Mathematical Modeling for the Discharge of a Metal Hydride Electrode," J. Electrochem. Soc., **142**, pp. 4006–4013.
[3] Smith, K., and Wang, C. Y., 2006, "Solid-State Diffusion Limitations on Pulse Operation of a Lithium-Ion Cell for Hybrid Electric Vehicles," J. Power Sources, **161**, pp. 628–639.
[4] Barbarisi, O., Vasca, F., and Glielmo, L., 2006 "State of Charge Kalman Filter Estimator for Automotive Batteries," Control Eng. Pract., **14**, pp. 267–275.
[5] Prins-Jansen, J. A., Fehribach, J. D., Hemmes, K., and de Wita, J. H. W., 1996, "A Three-Phase Homogeneous Model for Porous Electrodes in Molten-Carbonate Fuel Cells," J. Electrochem. Soc., **143**, pp. 1617–1628.
[6] Verbrugge, M. W., and Koch, B. J., 2003, "Electrochemical Analysis of Lithiated Graphite Anodes," J. Electrochem. Soc., **150**, pp. A374–A384.
[7] Newman, J., and Tiedemann, W., 1975, "Porous-Electrode Theory With Battery Applications," AIChE J., **21**, pp. 25–41.
[8] Fuller, T. F., Doyle, M., and Newman, J., 1994, "Simulation and Optimization of the Dual Lithium Ion Insertion Cell," J. Electrochem. Soc., **141**, pp. 1–10.
[9] Ramadass, P., Haran, B., Gomadam, P. M., White, R., and Popov, B. N., 2004, "Development of First Principles Capacity Fade Model for Li-Ion Cells," J. Electrochem. Soc., **151**, pp. A196–A203.
[10] Sikha, G., Popov, B. N., and White, R. E., 2004, "Effect of Porosity on the Capacity Fade of a Lithium-Ion Battery," J. Electrochem. Soc., **151**, pp. A1104–A1114.
[11] Wang, C. Y., Gu, W. B., and Liaw, B. Y., 1998, "Micro-Macroscopic Coupled Modeling of Batteries and Fuel Cells. Part I: Model Development," J. Electrochem. Soc., **145**, pp. 3407–3417.
[12] Wang, C. Y., Gu, W. B., and Liaw, B. Y., 1998, "Micro-Macroscopic Coupled Modeling of Batteries and Fuel Cells. Part II: Application to Ni-Cd and Ni-MH Cells," J. Electrochem. Soc., **145**, pp. 3418–3427.
[13] Gu, W. B., and Wang, C. Y., 2000, "Thermal and Electrochemical Coupled Modeling of a Lithium-Ion Cell," Proc.-Electrochem. Soc., **99**, pp. 748–762.
[14] Paxton, B., and Newmann, J., 1997, "Modeling of Nickel Metal Hydride," J. Electrochem. Soc., **144**, pp. 3818–3831.
[15] Verbrugge, M., and Tate, E., 2004, "Adaptive State of Charge Algorithm for Nickel Metal Hydride Batteries Including Hysteresis Phenomena," J. Power Sources, **126**, pp. 236–249.
[16] Hariprakasha, B., Marthaa, S. K., Jaikumara, A., and Shukla, A. K., 2004, "On-Line Monitoring of Leadacid Batteries by Galvanostatic Nondestructive Technique," J. Power Sources, **137**, pp. 128–133.
[17] Salkind, A. J., Fennie, C., Singh, P., Atwater, T., and Reisner, D. E., 1999, "Determination of State-of-Charge and State-of-Health of Batteries by Fuzzy Logic Methodology," J. Power Sources, **80**, pp. 293–300.
[18] Pop, V., Bergveld, H. J., Op het Veld, J. H. G., Regtien, P. P. L., Danilov, D., and Notten, P. H. L., 2006, "Modeling Battery Behavior for Accurate State-of-Charge Indication," J. Electrochem. Soc., **153**, pp. A2013–A2022.
[19] Smith, K., Rahn, C. D., and Wang, C. Y., 2007, "Control oriented 1D Electro-

chemical Model of Lithium Ion Battery," Energy Convers. Manage., **48**, pp. 2565–2578.
[20] Santhanagopalan, S., and White, R. E., 2006, "Online Estimation of the State of Charge of a Lithium Ion Cell," J. Power Sources, **161**, pp. 1346–1355.
[21] Haran, B. S., Popov, B. N., and White, R. E., 1998, "Determination of the Hydrogen Diffusion Coefficient in Metal Hydrides by Impedance Spectroscopy," J. Power Sources, **75**, pp. 56–63.
[22] Doyle, M., and Fuentes, Y., 2003, "Computer Simulations of a Lithium-Ion Polymer Battery and Implications for Higher Capacity Next-Generation Battery Designs," J. Electrochem. Soc., **150**, pp. A706–A713.
[23] Schiesser, W. E., 1991, *The Numerical Method of Lines: Integration of Partial Differential Equations*, Elsevier Science & Technology, Amsterdam, The Netherlands.
[24] 2003, FreedomCar Battery Test Manual for Power-Assist Hybrid Elecric Vehicles, DOE/ID-11069.
[25] Di Domenico, D., Fiengo, G., and Stefanopoulou, A., 2008, "Lithium-Ion Battery State of Charge Estimation With a Kalman Filter Based on a Electrochemical Model," Proceedings of the 2008 IEEE Conference on Control Applications, Vol. 1, pp. 702–707.
[26] Hermann, R., and Krener, A. J., 1977, "Nonlinear Controllability and Observability," IEEE Trans. Autom. Control, **22**, pp. 728–740.